PNAS RESEARCH ARTICLE | BIOPHYSICS AND COMPUTATIONAL BIOLOGY

Crowding limits relative bacterial surface accumulation with density-induced effective heating

Yaocai Liu[a,1], Rui He[a,1], Da Wei[b,1,2], Longfei Li[b,1], Mingcheng Yang[b,c,2], Junhua Yuan[a,2], and Yi Peng[b,c,2]

Affiliations are included on p. 7.

Edited by Raymond E. Goldstein, University of Cambridge, Cambridge, United Kingdom; received December 18, 2025; accepted September 7, 2026 by Editorial Board Member Paul Chaikin

The accumulation of microswimmers near walls has been studied for decades. While hydrodynamics and single-cell kinematics are well-explored, the role of cell-cell interactions remains understudied. However, in realistic, crowded environments such as the human gut, these interactions can be just as crucial. Here, we demonstrate that they actively weaken bacterial surface accumulation. Analysis of entrapped cell tracks reveals that crowding enhances orientational fluctuations, which increase the effective rotational diffusion and facilitate wall escape. A minimal model shows that this collective effect is equivalent to raising the system's effective temperature with density.

surface accumulation | biofouling | bacterial motility | microswimmer interaction

Significance

Bacterial surface accumulation initiates biofouling, compromising submerged materials and medical implants. While decades of research have focused on single-cell hydrodynamics and behavior, the role of cell-cell interactions—crucial in realistic, crowded environments such as the human gut—remains less understood. Here, we show that crowding inherently weakens relative surface accumulation. This collective effect is quantified experimentally and captured by a minimal model as an increased effective rotational noise, or effective heating. This effective noise serves as a simple, powerful descriptor for the many-body interactions governing the accumulation in dense active systems, bridging single-cell mechanics and population-level ecology. The insights apply readily to other microswimmer systems, including microbot-assisted drug delivery, where controlling surface accumulation helps achieve sufficient local dosage.

Materials submerged in aqueous environments become targets for microbial colonization within minutes (1, 2). Such microbial colonization is known as biofouling and results in undesirable consequences ranging from increased drag on ship hulls to infections on medical implants (1). Bacteria, as primary colonizers, quickly adhere to surfaces and initiate biofilm formation. This initial surface accumulation is the critical first step that creates a scaffold for secondary colonization by larger organisms (3).

Decades of research has sought to resolve the mechanisms of bacterial surface accumulation (4–8). Current research confirms that the accumulation of bacteria at interfaces arises from a competition between boundary-attracting and boundary-escaping mechanisms. Key factors promoting accumulation include the alignment effect during collisions between rod-shaped bacteria and walls (6, 9), hydrodynamic attraction arising from the force dipole component of the cell's flow field (5, 10), and biological surface appendages like fimbriae that enhance adhesion (11, 12). Conversely, active reorientation mechanisms such as bacterial tumbling (7), passive angular noise (13), and hydrodynamic effects of force quadrupole (14) facilitate escape from wall entrapment.

Despite this progress, a critical factor remains underexplored: the role of short-range cell-cell interactions—both steric and hydrodynamic—in wall escape. This gap stems from a research focus on elucidating individual bacterial behavior and near-surface fluid dynamics, which requires tracking cells at very low concentrations ($n \ll 0.1n_0$, where $n_0 = 8 \times 10^8$ cells/ml). As a benchmark, bacterial concentrations in the human gut are 0.1 to 1 n_0 (15, 16). While neglecting cell-cell interactions was justified in the dilute limit considered in earlier studies, understanding accumulation in a more realistic context (i.e., with abundant other microswimmers around) demands their inclusion. These close-range interactions may not only introduce reorientations that aid wall escape but also trigger complex behaviors like Lévy walks (17).

In this work, we investigate bacterial surface accumulation in chambers (thickness $H \approx 100$ μm) across two decades of concentrations (10^{-1} to 10^1 n_0). Interestingly, we find that surface accumulation quickly diminishes (i.e., the bulk becomes nearly equally populated) once the concentration exceeds ~1 n_0. To explore this phenomenon, we perform experiments with different bacterial strains, which vary in body length and tumbling behavior. Nevertheless, the density-induced weakening of relative surface accumulation is consistently observed. This density-induced effect is captured by an increasing effective temperature for cell-body rotation in a minimal model. These results strongly suggest that bacterial collisions, rather than individual motility traits or hydrodynamics, dominate boundary accumulation at concentrations exceeding 1 n_0. Our findings highlight that, in densely populated natural and industrial settings such as the gut and bioreactors, cell-cell interactions need to be considered as one of the primary factors in microbe-surface dynamics.

The authors declare no competing interest.

This article is a PNAS Direct Submission. R.E.G. is a guest editor invited by the Editorial Board.

Copyright © 2026 the Author(s). Published by PNAS. This article is distributed under Creative Commons Attribution-NonCommercial-NoDerivatives License 4.0 (CC BY-NC-ND).

[1]Y.L., R.H., D.W., and L.L. contributed equally to this work.

[2]To whom correspondence may be addressed. Email: weida@iphy.ac.cn, mcyang@iphy.ac.cn, jhyuan@ustc.edu.cn, or pengy@iphy.ac.cn.

This article contains supporting information online at https://www.pnas.org/lookup/suppl/doi:10.1073/pnas.2536051123/-/DCSupplemental.

Published October 29, 2026.

Downloaded from https://www.pnas.org by CAS INSTITUTE OF PHYSICS on October 30, 2026 from IP address 159.226.35.209.

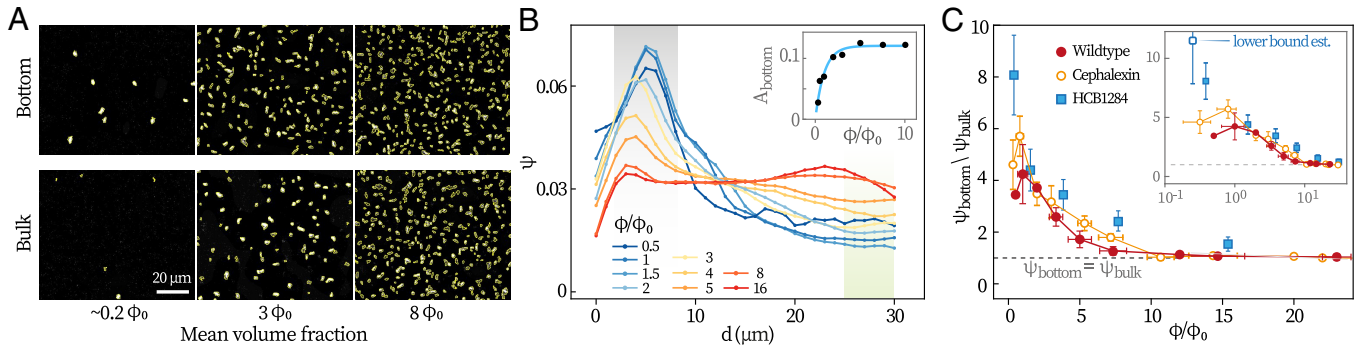


Fig. 1. Surface accumulation in bacterial suspensions of different densities. (*A*) Confocal microscopy images near the *Bottom* (*Upper* row) and near the *Center* (*Lower* row) at different bacterial concentrations ϕ. (*B*) The normalized area fraction ψ as a function of height d from the chamber bottom at varying ϕ. *Inset*: The 2D area fraction near the *Bottom*, A_{bottom}, versus ϕ. (*C*) Accumulation level characterized by $\psi_{\text{bottom}}/\psi_{\text{bulk}}$ for varying ϕ and bacterial strains, with the *Inset* presenting the same data on a semi-log scale. Markers and error bars represent the mean and SD from $N \geq 3$ experiments. The empty marker in the *Inset* indicates an estimated lower bound (measurements with effectively zero ψ_{bulk} excluded).

Results

Surface Accumulation Diminishes in Dense Suspensions. We observe bacterial suspensions in fluidic chambers using confocal microscopy. Videos at varying heights d from the bottom are acquired. Images are contrast-adjusted and binarized, and cells are detected via a thresholding algorithm (18) (*Materials and Methods*). Typical processed images are presented in Fig. 1*A*. The *Upper* and *Lower* rows show images taken near the bottom wall ($d \approx 3$ μm) and in the bulk ($d \approx 30$ μm), respectively. We observe that accumulation near the top and the bottom surfaces is qualitatively the same (14) but bottom images are clearer (especially under higher concentrations). We therefore focus on the region $d \in [0, d_0]$ near the bottom wall, with $d_0 = 30$ μm.

We examined suspensions of different bacterial strains at volume fractions ϕ ranging from 0.1 to 20 ϕ_0 (0.019% to 3.9%), where $\phi_0 = 0.19\%$ is the unit volume fraction corresponding to the unit number density n_0 for typical *Escherichia coli* cells. Before each experiment, ϕ is determined directly from optical density measurements. Because the number density n is more sensitive to cell size than ϕ, and the strains we use differ considerably in length, we adopt ϕ to characterize concentration hereafter (*Materials and Methods*).

We begin with wildtype *E. coli* cells. In dilute suspensions ($\phi \lesssim 3\phi_0$), bacteria accumulate near the no-slip walls, in agreement with previous reports (5, 6, 19). At very low densities (e.g., $\phi \approx 0.2\phi_0$), cells are heavily concentrated near the bottom, leaving the bulk nearly empty of cells (Fig. 1*A*). At an intermediate concentration (e.g., $\phi = 3\phi_0$), both the bulk and bottom become more populated, though the bottom remains denser; the visual difference between the two regions is less pronounced. In crowded suspensions (e.g., $\phi = 8\phi_0$), the bulk and bottom densities become indistinguishable. The vertical population distribution is characterized by $A(d)$, the absolute 2D area fraction of cell bodies at height d, and its normalized profile $\psi(d) \equiv A(d)/\int_0^{d_0} A(z)\mathrm{d}z$. Typical profiles of ψ are shown in Fig. 1*B*. The cell concentration peaks several μm above the bottom (gray shaded area in Fig. 1*B*). This is consistent with recent observations and is understood through a combination of the cells' hydrodynamic and steric interactions with the surface (14, 20–22). For clarity, values referenced for the bottom correspond to the maximum value within this bottom region, while values referenced for the bulk correspond to the mean for $d \in [25, 30]$ μm (green shaded in Fig. 1*B*).

In the dilute regime ($\phi \lesssim 3\phi_0$), the $\psi(d)$ profile remains qualitatively similar with increasing concentration ϕ (blue traces in Fig. 1*B*). Despite this stable normalized profile, the absolute area fraction in the bottom region, A_{bottom}, increases and saturates exponentially (Fig. 1 *B*, *Inset*). We further characterize surface accumulation by the ratio $\psi_{\text{bottom}}/\psi_{\text{bulk}}$ from the profile $\psi(d)$ (Fig. 1*C*), where a larger ratio indicates stronger accumulation. Consistently, this ratio is stable against varying ϕ in the dilute regime and diminishes in dense suspensions, see Fig. 1 *C*, *Inset*.

Note that the ratio $\psi_{\text{bottom}}/\psi_{\text{bulk}}$ quantifies surface accumulation in a relative sense; its decrease in dense suspensions reflects that the bulk becomes increasingly populated as the surface saturates, consistent with the observations in Fig. 1*A*. This trend follows a clear physical logic. When the surface becomes crowded, enhanced cell-cell interactions could significantly facilitate cell reorientation, increasing the detachment rate. Consequently, surface accumulation weakens, yielding a more homogeneous distribution.

We hypothesize that the stable trend of $\psi_{\text{bottom}}/\psi_{\text{bulk}}$ in the dilute regime arises because density-induced detachment is negligible compared to the baseline rate from single-cell tumbling, a dominant mechanism in extremely dilute suspensions (4, 8, 19).

To test this hypothesis, we examine surface accumulation in tumble-free *E. coli* (HCB1284; see *Materials and Methods*), shown as blue data in Fig. 1*C*. These cells display a monotonic decrease of $\psi_{\text{bottom}}/\psi_{\text{bulk}}$ with ϕ: accumulation is strongest in the most dilute suspensions. For $\phi \leq 0.2\phi_0$, the bulk is often empty within our observation span, resulting in an effectively infinite $\psi_{\text{bottom}}/\psi_{\text{bulk}}$. These data are excluded from the reported statistics since the ratio is undefined when the bulk contains no cell; the corresponding lower bound is shown as an open marker in Fig. 1 *C*, *Inset*. The results support our hypothesis: when the baseline detachment rate provided by single-cell tumbling is absent, increasing density consistently boosts detachment and hence weakens surface accumulation.

The tumble-free strain is longer (3.5 ± 1.2 μm, mean ± SD) than the wildtype (2.8 ± 0.6 μm).* To ensure this size difference does not cause the different $\psi_{\text{bottom}}/\psi_{\text{bulk}}$ trend, we study drug-elongated wildtype cells. A mild dose of cephalexin is applied to bacteria (*Materials and Methods*) and yields cells of lengths

*Although the mean body length of HCB1284 with mCherry inserts (3.5 μm) is only 25% longer than the wildtype (2.8 μm), the former has larger variability (1.2 μm SD) than the latter (0.6 μm), resulting in that the smooth swimming bacterial suspensions contain much larger fractions of long cells than wildtype suspensions contain.

Downloaded from https://www.pnas.org by CAS INSTITUTE OF PHYSICS on October 30, 2026 from IP address 159.226.35.209.

6.0 ± 1.3 μm. We confirm that their swimming speed and tumble behaviors are unaffected—though their angular persistence after tumbling is stronger. The surface accumulation of these elongated cells (orange data in Fig. 1*C*) remains qualitatively the same as wildtype.

Angular Kinematics of Entrapped Bacterial Motion. We next study the dynamics of bacteria swimming near surfaces to obtain a microscopic perspective on how cell-cell interactions affect surface accumulation. Since a cell's entrapment at and escape from the wall are dictated by its swimming angle, we focus on the angular kinematics of entrapped cells. A cell is considered entrapped if it continuously remains within $d \leq 5$ μm of the bottom (*Materials and Methods*).

We first characterize the in-plane angular noise by the effective rotational diffusivity $D_{r,xy}$. Entrapped cells are tracked, and from the track direction $\theta_{xy}(t)$ (Fig. 2*A*), we compute the mean square angular displacement (MSAD). For a purely diffusive process, MSAD scales linearly with the time interval δt ($\sim 2\, D_{r,xy}\delta t$). However, due to hydrodynamic wall effects, entrapped cells swim in circular paths near the surface (23), which introduces a convective contribution $d\theta_{xy} \sim \omega_{\mathrm{circ}}\delta t$ and hence a quadratic term in the MSAD. Here ω_{circ} is the constant angular speed of circular swimming. To isolate the contribution of diffusion, we fit the MSAD quadratically to $\omega_{\mathrm{circ}}^2\delta t^2 + 2D_{r,xy}\delta t + \mathrm{const.}$ and extract $D_{r,xy}$ from the coefficient of the linear term; see *Materials and Methods*. This method consistently captures experimental results; a comparison with alternative methods is provided in *SI Appendix*.

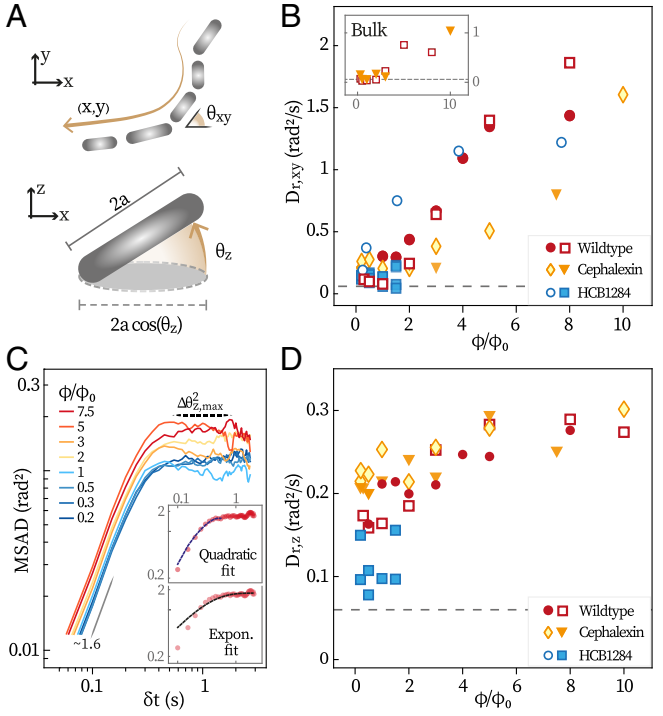


Fig. 2. Angular noise of bacteria near a surface. (*A*) Schematic of cell tracking in the *xy*-plane (*Top*) and how polar angle θ_z can be inferred from apparent length (*Bottom*). (*B*) In-plane rotational diffusivity, $D_{r,xy}$, as a function of ϕ. Different symbols denote different experiments; *Inset* shows bulk measurements. (*C*) Mean square angular displacement (MSAD) of θ_z across concentrations. *Insets* illustrate the two methods for extracting the polar rotational diffusivity $D_{r,z}$ (*Materials and Methods*). (*D*) $D_{r,z}$ as a function of ϕ. Dashed lines in (*B* and *D*) indicate the thermal background of 0.06 rad^2/s.

Fig. 2*B* displays results of different strains. For all strains, $D_{r,xy}$ increases with ϕ, showing an approximately linear dependence. Bulk measurements yield quantitatively similar results (Fig. 2 *B*, *Inset*). In the dilute limit, all strains approach the background thermal noise, estimated as $k_BT/8\pi\eta a^3 = 0.06$ rad^2/s for a passive particle (13), where k_B is the Boltzmann constant, T is room temperature, η is the viscosity of water, and $a = 1.5$ μm is a typical bacterial half-length.

Compared to the in-plane angular kinematics, kinematics of the polar angle (θ_z in Fig. 2 *A*, *Lower* panel) is more directly involved in wall entrapment and detachment (7, 14, 22). However, tracking the evolution of θ_z is challenging, especially in crowded environments. Here, we employ an approximate yet effective technique to address this issue. When tracking the cells' motion in the *xy*-plane, we also record their 2D-projected length in real-time as $L(t)$, which is related to θ_z as $L(t) = 2a\cos\theta_z$ (Fig. 2 *A*, *Lower* panel). For each individual cell, its length $2a$ is approximated as the maximum value of $L(t)$, denoted as $L_{\max}$. Note that, as $L_{\max} \leq 2a$, results obtained by this method tend to overestimate θ_z; and longer cell bodies lessen this relative error.

We track θ_z from eligible entrapped tracks (*Materials and Methods*) and compute the corresponding MSAD. Representative data for elongated wildtype cells at varying densities are displayed in Fig. 2*C*. At short time intervals ($\delta t \leq 0.3$ s), MSAD exhibits superdiffusive scaling with time across all ϕ. At longer time scales, the MSAD plateaus at a value $\Delta\theta_{z,\max}^2$ that increases with ϕ, where $\Delta\theta_{z,\max}$ corresponds to the maximum polar angle variation allowed for entrapped cells.

The superdiffusivity primarily arises from the cell body wobbling. When a bacterium swims, its cell body counter-rotates against its flagellar bundle, causing the polar angle θ_z to vary with time approximately sinusoidally: $d\theta_z \sim \sin(\omega_{\mathrm{wob}}\delta t)$, where ω_{wob} is the wobbling frequency (see detailed experimental measurements in refs. 7 and 24). At short times, this yields a convective dependence ($d\theta_z \sim \omega_{\mathrm{wob}}\delta t$) in addition to the existing angular diffusion in θ_z, culminating in the observed superdiffusive behavior of the MSAD. Note that this coexistence of convective and diffusive angular variations is analogous to the case of $D_{r,xy}$, justifying the use of the same protocol to extract the rotational diffusion coefficient $D_{r,z}$. We thus perform quadratic polynomial fitting up to the plateau to obtain $D_{r,z}$ (Fig. 2 *C*, *Upper Inset*). Results across strains are displayed in Fig. 2*D*.

The information given by wall entrapment, i.e., the plateaus at longer times of MSAD, provides a complementary view and corroborates the measured $D_{r,z}$. To characterize this feature, which quadratic fitting cannot capture, we simply approximate the wall entrapment as a harmonic potential in θ_z (*Materials and Methods*). This approximation predicts MSAD to exhibit an exponential saturation—from which $D_{r,z}$ can also be extracted (Fig. 2 *C*, *Lower Inset*). Results from both methods agree well, differing by only ~10%. We report $D_{r,z}$ from the quadratic polynomial fit for methodological consistency with $D_{r,xy}$ (see *SI Appendix* for details). Like $D_{r,xy}$, $D_{r,z}$ increases with ϕ but with a slower trend (Fig. 2*D*). At high concentrations, $D_{r,z}$ amounts to ~20% of $D_{r,xy}$. Note that because cells with the strongest fluctuations tend to escape and are not sampled, our results represent a lower bound for the actual $D_{r,z}$ near the surface. These results directly show how surface crowdedness intensifies polar angle fluctuations.

We further substantiate the polar angle kinematics with more straightforward statistics of θ_z. For $\theta_z(t)$ of each entrapped track, we compute its mean $\overline{\theta}z$ and SD σ_z over time (Fig. 3*A*) and examine their distributions across concentrations. Representative

Downloaded from https://www.pnas.org by CAS INSTITUTE OF PHYSICS on October 30, 2026 from IP address 159.226.35.209.

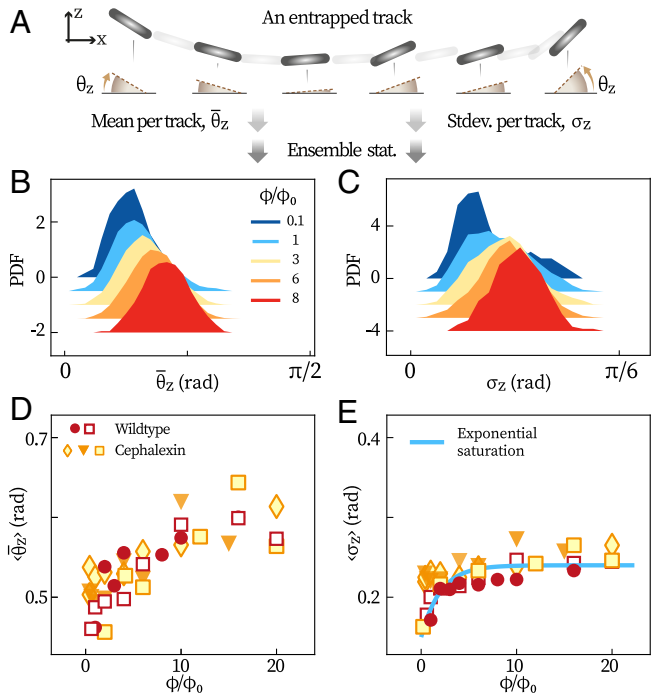


Fig. 3. Polar angle fluctuation of bacteria near a surface. (*A*) Definition of metrics: $\bar{\theta}_z$ and σ_z denote the temporal mean and SD of θ_z for an individual track. Probability distributions of $\bar{\theta}_z$ (*B*) and σ_z (*C*) for different concentrations; data are vertically offset for clarity. (*D* and *E*) Ensemble averages $\langle\bar{\theta}_z\rangle$ and $\langle\sigma_z\rangle$ corresponding to the distributions in (*B* and *C*), respectively. Symbols represent different experiments. The blue line in (*E*) is an exponential saturation with the same characteristic rate as in Fig. 1 *B*, *Inset*.

data for elongated cells are displayed in Fig. 3 *B* and *C*, with each distribution comprising $O(10^2$–$10^3)$ tracks. Consistent with the increase of $D_{r,z}$ with ϕ (Fig. 2*D*), entrapped cells experience stronger fluctuations in θ_z at higher concentrations, as seen in the right-shifting distributions of σ_z in Fig. 3*C*. Meanwhile, we find that entrapped cells also swim with a more tilted orientation (larger $\bar{\theta}_z$) at higher concentrations (Fig. 3*B*). The increasing trends of $\langle\bar{\theta}_z\rangle$ and $\langle\sigma_z\rangle$ with ϕ are shown in Fig. 3 *D* and *E*, respectively, where $\langle\cdot\rangle$ denotes the ensemble average. Data for non-elongated wildtype cells (red symbols) exhibit qualitatively the same trend. Interestingly, the saturation of $\langle\sigma_z\rangle$ with ϕ appears to follow a similar exponential form (blue line in Fig. 3*E*) as that of A_{bottom} (Fig. 1 *B*, *Inset*). In other words, the crowdedness of the surface appears to enhance its dwellers' polar angle fluctuation proportionally.

Modeling Results. A minimal mean-field model successfully captures how bacterial density affects surface accumulation. Density-induced effects are encompassed by an increasing effective temperature for cell-body rotation. Bacteria are modeled as active Brownian particles (ABPs) in the xz-plane, confined between no-slip walls at $z = 0$ and H (Fig. 4*A*), with periodic boundary conditions along the x-axis (length W). They are subject to a rotational white noise whose intensity increases with cell density. The model includes far-field hydrodynamic interactions (HI) and steric exclusion between the cell and the wall. Each particle is described by its position $\boldsymbol{r} = (x, z)$ and orientation $\hat{\boldsymbol{e}} = (-\sin\alpha, -\cos\alpha)$ (for left-moving particles). The angle α represents an adjusted polar angle: $\alpha = \pi/2 - \theta_z$ for cells approaching the surface (Fig. 4*A*) and $\alpha = \pi/2 + \theta_z$ for cells leaving (Fig. 4 *A*, *Inset*). The ABP kinematics are governed by:

$$\begin{aligned}\dot{\boldsymbol{r}} &= v_0\hat{\boldsymbol{e}} + u_z(\alpha, z)\hat{\boldsymbol{z}} - \tfrac{1}{\gamma_T}\nabla_{\boldsymbol{r}}U;\\ \dot{\alpha} &= -\Omega(\alpha, z) + \sqrt{2D_{r,z}}\xi.\end{aligned} \quad [1]$$

Here, v_0 is the constant self-propulsion speed. Note that the particle's actual speed also includes contributions from steric and hydrodynamic interactions, and thus differs from v_0. u_z is the HI-induced velocity along the z-axis (unit vector $\hat{\boldsymbol{z}}$), γ_T is the translational drag coefficient, and U is a short-range potential for steric wall exclusion. Ω is the HI-induced angular velocity, and ξ is a Gaussian white noise with $\langle\xi(t)\rangle = 0$ and $\langle\xi(t)\xi(t')\rangle = \delta(t - t')$, where $\delta(\cdot)$ is the Dirac delta function.

Hydrodynamic interactions between the particle and the wall are approximated by modeling the particle as a force dipole p following ref. 5:

$$\begin{aligned}u_z &= -\tfrac{3p}{64\pi\eta z^2}(1 - 3\cos^2\alpha),\\ \Omega &= -\tfrac{3p\cos\alpha\sin\alpha}{64\pi\eta z^3}\left[1 + \tfrac{1}{2}\tfrac{\epsilon^2-1}{\epsilon^2+1}(1+\cos^2\alpha)\right],\end{aligned} \quad [2]$$

where ϵ is the particle aspect ratio. These expressions describe interactions near the bottom wall; for the top wall, z is replaced by $H - z$ and the z-component of $\hat{\boldsymbol{e}}$ is reversed.

The particle further interacts with the wall through steric exclusion and wall alignment. Steric exclusion is implemented via a short-range harmonic potential $U(d) = K(d - \ell)^2/2$ for $d < \ell$ (zero otherwise), where ℓ is the characteristic length for steric interactions and approximates the bacterial body width. Wall alignment is modeled by resetting the polar angle α to $\pi/2$ when $d < \ell$ and $\alpha < \pi/2$. For more numerical details see *Materials and Methods*.

Finally, density-induced effects are incorporated via a mean-field rotational noise $D_r(\phi) = D_{r0} + \beta\phi/\phi_0$, where the slope β quantifies the noise increase per unit bacterial density. The linear dependence of D_r on ϕ is a first-order approximation based on our experimental measurements near the surface and in the bulk (Fig. 2*B*), yielding $\beta \sim 0.1$ rad^2 s^{-1}. This approximation is also supported by particle-based simulations of self-propelled rods (SPRs). The simulations show that far-field hydrodynamic interactions (dominant in the dilute regime) and steric collisions (dominant in the dense regime) each yield a (near-)linear dependence (*SI Appendix*, Fig. S5). Further simulation details of the SPR model are provided in *Materials and Methods*.

The weakening of surface accumulation with density is captured by our model. With typical parameters—$a = 2$ μm, $v_0 = 20$ μm/s, $P = 0.6$ pN·μm (9), $H = 100$ μm, $D_{r0} = 0.4$ rad^2 s^{-1}, and $\beta = 0.51$ rad^2 s^{-1}—the model reproduces the evolution of $\psi(d)$ with ϕ: from a peak near the surface to a nearly flat distribution (Fig. 4*B*). Furthermore, by adjusting only the noise-density coupling strength β, the model reproduces the distinct trends for all strains (Fig. 4*C*). The results reasonably show that β is highest for the normal-sized wildtype and lowest for the tumble-free strain. The model also provides reasonable predictions for the residence time τ_{res} of the tumble-free strain at low concentrations. The best fit to measurements is $D_{r0} = 0.1$ rad^2 s^{-1} and $\beta = 0.15$ rad^2 s^{-1}. At $\phi = 0.25$, 0.4, and 1.5 ϕ_0, the modeled (measured) values are: $\tau_{\text{res}} = 21.1$ s (23.7 s), 13.4 s (7.4 s), and 3.1 s (3.1 s), respectively.

In the minimal model, the increase of D_r with density is imposed rather than derived. To examine the robustness of the minimal model, and to explore its microscopic basis, we consider three classes of extended models (*SI Appendix*).

Downloaded from https://www.pnas.org by CAS INSTITUTE OF PHYSICS on October 30, 2026 from IP address 159.226.35.209.

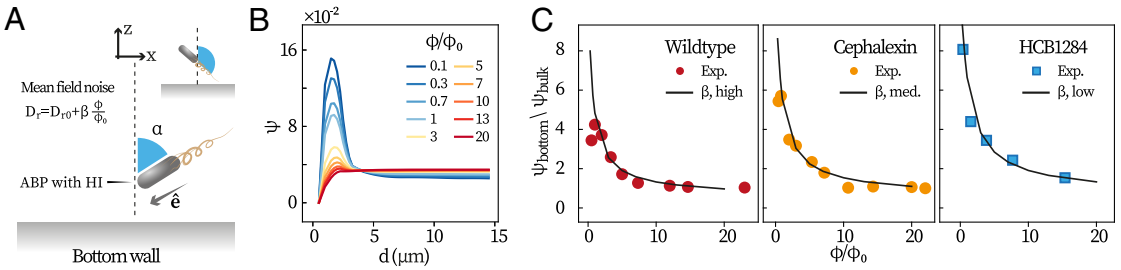


Fig. 4. Modeling results. (*A*) Schematic of the model, defining the adjusted polar angle $\alpha = \pi/2 - \theta_Z$ for cells approaching the surface and $\alpha = \pi/2 + \theta_Z$ for departing cells (*Inset*). (*B*) Normalized distribution $\psi(d)$ at different concentrations. (*C*) Surface accumulation ratio $\psi_{\text{bottom}}/\psi_{\text{bulk}}$ from simulations with different noise-density coupling strengths β. Symbols are experimental data; the baseline rotational diffusivity is $D_{r0} = 0.4$ rad^2 s^{-1} for all simulations; β =0.51, 0.38, and 0.26 for panels in (*C*) from *Left* to *Right*, respectively.

First, free-space simulations model bacteria as hydrodynamically interacting force dipoles, as sterically interacting SPRs (each rod is a rigid two-sphere dimer with anisotropic friction), or as rods subject to both hydrodynamic and steric interactions; these test whether the interactions alone, without wall confinement, produce the linear increase of D_r with density (*SI Appendix*, Fig. S5). Second, a mean-field SPR model, with wall repulsion and alignment generated by dimer-wall contact while $D_r(\phi)$ remains assigned, tests the role of finite particle geometry (*SI Appendix*, Fig. S6). Third, near-wall multiparticle simulations explicitly include pairwise hydrodynamic interactions and wall-image flows, with or without a short-range cell-cell scattering torque (*SI Appendix*, Fig. S7). In these simulations, the intrinsic single-particle diffusivity D_{r0} is held fixed, and the density-dependent effective rotational noise emerges from interactions rather than being prescribed (*SI Appendix*, Fig. S7). These models show consistent results. In free space, hydrodynamic interactions, steric collisions, and their combination each produce a near-linear increase of the effective rotational diffusivity with density (*SI Appendix*, Fig. S5), supporting the first-order closure $D_r = D_{r0} + \beta\phi/\phi_0$. The SPR model preserves the qualitative decay of relative surface accumulation, showing that the result is insensitive to finite rod geometry and the detailed implementation of wall alignment (*SI Appendix*, Fig. S6). More directly, the near-wall multiparticle simulations reproduce the decay of $\psi_{\text{bottom}}/\psi_{\text{bulk}}$ without imposing a density-dependent D_r (*SI Appendix*, Fig. S7). Finally, the decay trends for all three experimental strains and all model classes are qualitatively the same (*SI Appendix*, Fig. S8). These results indicate that different microscopic mechanisms can be coarse-grained into a common effective heating mechanism in the rotational degree of freedom, while the microscopic details mainly determine how strongly density enhances that noise. The minimal model captures this mechanism in its simplest form, which also underpins its general applicability.

Discussion

Our study reveals that bacterial surface accumulation weakens significantly as concentrations increase beyond the dilute regime. This transition marks a shift from a state governed by single-cell tumbling to one dominated by density-induced collective interactions. Crucially, the net effect of these complex interactions can be semi-quantitatively captured by a single parameter—an enhanced effective rotational noise in a minimal mean-field model.

This density-dependent mechanism is often overlooked in studies focusing solely on single-cell hydrodynamics, yet it is critical for predicting accumulation under realistic, crowded conditions such as in the human gut. Quantitatively, our results establish that peer interaction becomes the governing mechanism of bacterial surface accumulation for $\phi \gtrsim 1.0\ \phi_0$ (Fig. 1 *C* and *Inset*). In this regime, our data support the following picture: as density increases, the surface population saturates (Fig. 1 *B*, *Inset*) while the bulk gradually fills, homogenizing the overall distribution and reducing relative surface accumulation ($\psi_{\text{bottom}}/\psi_{\text{bulk}}$). The characteristic scale for this exponential saturation is also approximately 1.0 ϕ_0, as evidenced by both population and noise level data (Figs. 1 *B*, *Inset* and 3*E*).

Some remarks are necessary regarding the highly simplified model we employ. Several detailed known mechanisms are deliberately omitted, including near-field hydrodynamics beyond the dipole approximation (25–27), cell body wobbling (24), and flagellar hook flexibility (28). Nevertheless, the model proves effective. This effectiveness underscores a key insight: in dense suspensions, the effects of the neglected mechanisms, combined with frequent cell-cell interactions (e.g., collisions), reduce to the effect of a simple white noise. This reduction is analogous to a central limit theorem for reorientation kinematics, making a mean-field enhancement of rotational noise a powerful and sufficient descriptor for population-level behavior. Although the modeling results are quantitatively reasonable, we emphasize that the model's primary aim is to provide qualitative insight into surface accumulation in dense suspensions.

This framework applies broadly to other microswimmers, such as algae, sperm, and artificial microbots, where particle geometry and flow fields can be more complex and single-particle behavior more elusive. Our results suggest that such complexity can be dissolved in many-body interactions, advancing understanding of surface accumulation in general. The common decay trend of the accumulation ratio across strains and models (*SI Appendix*, Fig. S8) further suggests that the effective heating in the rotational degree of freedom is a generic consequence of crowding, largely independent of the microscopic details of the interactions. This has important implications for microswimmer-based applications. For example, in microbot-assisted drug delivery, surface accumulation of drug-loaded particles promotes wall-assisted transport (29) and enables sufficient local dosage (30); understanding and modulating this accumulation is therefore of key interest.

Materials and Methods

Bacteria Culture. *E. coli* strain HCB1284 and BW25113 are used for this study. Smooth swimming strain HCB1284 (Δ*CheY*) is transformed with pBAD33 *flic* and pTrc99a mCherry or only transformed with pBAD33 *flic*. Bacteria is cultured in TB medium with appropriate antibiotics (25 μg/ml chloramphenicol,

Downloaded from https://www.pnas.org by CAS INSTITUTE OF PHYSICS on October 30, 2026 from IP address 159.226.35.209.

100 μg/ml ampicillin) at 33 °C to an optical density (OD, 600 nm wavelength) of 0.51. Arabinose with final concentration of $0.01\%(w/w)$ is added to express extra flagella at the beginning of the culture and IPTG with final concentration of 100 μM were added at OD of 0.23 to express mCherry.

The wildtype strain BW25113 expresses green fluorescent protein. This strain is first cultured overnight at 37.0 °C in TB medium, shaken at 200 rpm. The saturated culture is diluted 100 fold in fresh TB medium and incubated at 30 °C under identical shaking conditions. After 6.5 h, bacteria are harvested by centrifugation (1,000 or 800×g, 5 min), washed, and resuspended in motility buffer (MB) (10 mM potassium phosphate, 67 mM NaCl, and 0.1 mM EDTA). To induce cell elongation, cephalexin (Solarbio Inc., ∼30 μg/ml) is added, 3.5 h after the start of the fresh culture. The resulting cells exhibit body lengths of 6.0 ± 1.3 μm (mean ± SD).

Volume Fill Fraction. Concentration of bacterial suspensions is determined by measuring the optical density at 600 nm (OD_{600}), which primarily reflects the volume fraction of cell bodies. For wild-type *E. coli* (considered as a cylinder of length $2a = 3$ μm and diameter $2b = 1$ μm), an $OD_{600} = 1$ corresponds to a number density $n = 8 \times 10^8$ cells/ml $\equiv n_0$ and a volume fraction $\phi = n{\cdot}2\pi ab^2 = 0.19\% \equiv \phi_0$. Because bacterial strains of varying lengths are used, and their number density varies at the same OD_{600}, we use ϕ to characterize concentration. In experiments, after centrifugation, dense suspensions reach $\phi = 40$ to $80\,\phi_0$, which are then diluted to working concentrations of 0.1 to $20\,\phi_0$; beyond this range, bacterial turbulence emerges (27).

Observation. Suspensions of the strain BW25113 of varying concentrations are filled into flow chambers and sealed with UV-cured glue (NOA81). Chambers are custom made ($H \approx 85$ μm) with a slide and a coverslip spaced by double-sided tape. Confocal microscopy is performed at varying heights d (resolution 1 μm) from the bottom walls with a Prime-95B camera at a frame rate of 20 fps. A 40× objective is used (0.275 μm/pixel).

The observation chambers for the smooth swimming strain HCB1284 are fabricated by attaching a PDMS sheet to a coverslip with double-sided tapes. The resultant chamber depth is 100 μm. The same strain with or without mCherry are mixed in different ratios, allowing us to inspect single-cell dynamics even in dense suspensions. Before observation, samples are placed on the stage for 5 min to reach steady state. Nikon confocal microscopy equipped with a 40× water immersion objective (NA 1.15, 0.275 μm/pixel) is used to obtain the image every 1 μm from the bottom of the chamber. For measuring the residence time of the bacteria staying at surface, we used Nikon Ti-E microscopy equipped with a 561 nm laser and a 40x objective (NA 0.6); the videos were recorded at a frame rate of 25 fps with a scientific CMOS camera (Photometric kinetix).

Image Processing. We apply a band-pass filter (3 to 50 px) to the confocal images to get rid of the background pixel intensity variation as well as the salt and pepper noise. The image is then adjusted by histogram saturation and binarized before further analysis such as cell detection.

After binarization, the number of occupied pixel N_{occu} reports the two dimensional (2D) fill ratio (by bacterial cell bodies) within the imaging plane $A(d)$, as $A(d) \equiv \langle N_{\text{occu}} \rangle / N_{\text{field}}$. Here $\langle\cdot\rangle$ represents average over $\mathcal{O}(10^2)$ frames of images. N_{occu} is computed as the total area enclosed by detected cell body contours. Contours shorter than 9 px (corresponding to the typical cross-sectional size of a bacterium) are considered noise and excluded. N_{field} is the total number of the pixels per image. From $A(d)$, the scaled probability density function (PDF) $\psi(d) \equiv A(d) / \int_0^{d_0} A(z)\mathrm{d}z$ is computed.

Cell detection and tracking are performed with the TrackMate plugin in ImageJ (18). Further analyses (e.g., curvature, diffusion, etc.) are carried out with custom Python programs.

Definitions of θ_{xy} and θ_z. Videos used for obtaining single-cell kinematics near the bottom surface are recorded at 20 to 25 fps. Recordings last 5 s or 30 s. θ_{xy} is defined based on a cell's 2D track. An eligible track for the analysis of MSAD must 1) last longer than 1.0 s–which ensures meaningful temporal analysis; and 2) have a mean speed of more than 5 μm/s–which excludes stuck and dead cells. Using the cell's body orientation $\theta_{xy}^{\text{body}}$ changes the rotational diffusivity $D_{r,xy}$ obtained negligibly (*SI Appendix*). We therefore have opted for using θ_{xy}.

Meanwhile, the polar angle θ_z is defined as the included angle between the long axis of the cell body and the bottom surface. A tracks is eligible for statistical analysis if it meets all three of the following criteria: 1) lasts longer than 0.5 s; 2) has a mean speed more than 5 μm/s; and 3) has at least an aspect ratio of 3–which guarantees the accuracy of detecting the cell's body orientation.

Extracting $D_{r,xy}$. Consider a surface-entrapped bacterium swimming circularly at an angular speed ω_{circ} and subjected to an in-plane rotational diffusivity $D_{r,xy}$. Over a time interval δt, its measured directional change is $d\theta_{xy} = \omega_{\text{circ}}\delta t + \delta\theta_{xy} + \zeta$, where $\delta\theta_{xy}$ is the diffusive angular change and satisfies $\langle \delta\theta_{xy}^2 \rangle = 2D_{r,xy}\delta t$, and ζ denotes measurement uncertainty. Assuming the three terms are uncorrelated, the MSAD reads $\langle d\theta_{xy}^2 \rangle = \omega_{\text{circ}}^2\delta t^2 + \langle \delta\theta_{xy}^2 \rangle + \langle \zeta^2 \rangle = \omega_{\text{circ}}^2\delta t^2 + 2D_{r,xy}\delta t + \text{Const.}$, where $\langle\cdot\rangle$ denotes ensemble average. $D_{r,xy}$ is taken as half the linear coefficient from a least-square quadratic polynomial fitting. For more details of fitting methods, see *SI Appendix*.

Extracting $D_{r,z}$. The quadratic polynomial fitting approach is also applied to obtain $D_{r,z}$. In this case, the MSAD in the small-to-intermediate time scales (i.e., before MSAD plateaus) is fitted to $\langle d\theta_z^2 \rangle = \omega_{\text{circ}}^2\delta t^2 + 2D_{r,z}\delta t + \text{Const.}$, where ω_{wob} denotes the angular speed of cell body wobbling projected onto the xz-plane.

Meanwhile, to exploit information on the long time scales (the plateaued regime), we develop a model that helps extracting $D_{r,z}$ by exponential fitting. In this model, the wall entrapment is approximated as a harmonic potential that exerts a recovery torque on θ_z:

$$\gamma\dot{\theta}_z = -k(\theta_z - \Theta_z) + \xi_z. \qquad [3]$$

Here k denotes the stiffness of the harmonic potential, γ is the rotational drag coefficient of a bacterium within xz-plane, Θ_z is the equilibrium position, and ξ_z is a white noise. ξ_z satisfies $\langle \xi_z(t)\xi_z(t') \rangle = 2D_{r,z}\gamma^2\delta(t-t')$ with $\delta(\cdot)$ the Dirac delta function. By definition, MSAD $\equiv \langle [\theta_z - \theta_z(0)]^2 \rangle$, we first integrate Eq. **3** from $t' = 0$ to $t' = t$ to obtain an analytic expression for $\theta_z(t) - \theta_z(0)$; and then perform ensemble average on the square of the terms. With $\langle \xi_z \rangle = 0$, $\langle \theta_z(0) \rangle = \Theta_z$, and the expression of $\langle \xi_z(t)\xi_z(t') \rangle$, we obtain the expression describing the saturating profile:

$$\text{MSAD} = D_{r,z}\,\tau(1 - e^{\frac{-2\delta t}{\tau}}), \qquad [4]$$

with $\tau = \gamma/k$ the characteristic time scale of MSAD saturation. τ and $D_{r,z}$ are the only two fitting parameters in this approach. One may further include cell body wobbling into Eq. **3** but we find that the fitting results change negligibly.

Numerical Details of the Minimal Modeling. Simulation parameters are set based on experimental measurements. The simulation box dimensions are $W \times H = 100 \times 100$ μm, and the fluid viscosity is $\eta = 0.89$ mPa·s. the self-propulsion speed is $v_0 = 20$ μm/s, the force dipole strength is $P = 0.6$ pN·μm (9), and the aspect ratio is $\epsilon = 5$. For simplicity, anisotropy in the translational friction coefficient γ_T induced by the cell body shape is neglected; γ_T is approximated as that of a sphere of effective radius $r = 2$ μm, i.e., $\gamma_T = 6\pi\eta r$. For computational efficiency, hydrodynamic interactions are computed only for $d < 0.15H$ from each wall (i.e., a total region of $0.3H$ across the channel height); varying this cutoff from $0.06H$ to $0.3H$ affects the numerical results negligibly (<10%). For computing steric interactions, the wall steric potential stiffness is $K = 10$ pN/μm, and the characteristic length for steric interactions is $\ell = 1.2$ μm.

Simulation Details of SPR Suspensions. Particle-based SPR simulations are performed to rationalize the linear dependence of the effective rotational diffusivity D_r on ϕ used in the minimal mean-field model. SPR suspensions are simulated under periodic boundary conditions. Each SPR (representing a bacterium) is modeled as a hard-sphere dimer with a self-propulsion velocity v_0,

Downloaded from https://www.pnas.org by CAS INSTITUTE OF PHYSICS on October 30, 2026 from IP address 159.226.35.209.

with a force dipole of strength p embedded along its swimming orientation $\hat{\boldsymbol{e}}$. The equations of motion for particle i are

$$\dot{\boldsymbol{r}}_i = v_0\hat{\boldsymbol{e}}_i + \sum_{j\neq i}\boldsymbol{u}(\boldsymbol{r}_{ij}) + \boldsymbol{\Gamma}^{-1}\left[-\sum_{j\neq i}\nabla_{\boldsymbol{r}_i}U(\boldsymbol{r}_{ij})\right]; \quad [5]$$

$$\dot{\hat{\boldsymbol{e}}}_i = \left[\frac{1}{\gamma_r}\sum_{j\neq i}\boldsymbol{M}_{ij} + \sum_{j\neq i}\boldsymbol{\omega}(\boldsymbol{r}_{ij}) + \sqrt{2D_{r0}}\boldsymbol{\xi}_i\right]\times\hat{\boldsymbol{e}}_i. \quad [6]$$

Here, the anisotropy of the SPR is incorporated through the translational friction tensor $\boldsymbol{\Gamma} = \gamma_{\parallel}\hat{\boldsymbol{e}}\hat{\boldsymbol{e}} + \gamma_{\perp}(\mathbf{I} - \hat{\boldsymbol{e}}\hat{\boldsymbol{e}})$, where $\gamma_{\parallel}$ and $\gamma_{\perp}$ represent the translational friction coefficients parallel and perpendicular to the rod's long axis, respectively. The far-field flow $\boldsymbol{u}(\boldsymbol{r}_{ij})$ generated by dipole j advects particle i, and the associated angular velocity $\boldsymbol{\omega}(\boldsymbol{r}_{ij})$ perturbs the orientation of particle i. In addition, the steric collisions described by $U(\boldsymbol{r}_{ij})$ among anisotropic SPRs generate torques $\boldsymbol{M}_{ij}$ that further reorient particle i. Finally, γ_r denotes the rotational friction coefficient, $D_{r0} = 1/\gamma_r$ is the intrinsic rotational diffusivity of an isolated particle, and $\boldsymbol{\xi}_i$ is Gaussian white noise satisfying $\langle\boldsymbol{\xi}_i\rangle = \mathbf{0}$ and $\langle\boldsymbol{\xi}_i(t)\boldsymbol{\xi}_j(t')\rangle = \mathbf{I}\delta_{ij}\delta(t-t')$. The simulations show that D_r increases approximately linearly with ϕ. Single-SPR modeling in the mean-field fashion and many-particle SPR simulations with hydrodynamic interactions switched off are also performed. Further details are provided in *SI Appendix*.

Data, Materials, and Software Availability. Data used in the study are available in an open data repository (31).

ACKNOWLEDGMENTS. This work was supported by Fundamental and Interdisciplinary Disciplines Breakthrough Plan of the Ministry of Education of China (JYB2025XDXM502) and National Natural Science Foundation of China Grants (12574238, 12090053, T2325027, 12274448, T2221001, and 12474206).

Author affiliations: [a]Hefei National Research Center for Physical Sciences at the Microscale, University of Science and Technology of China, Hefei 230026, Anhui, China; [b]Beijing National Laboratory for Condensed Matter Physics, Institute of Physics, Chinese Academy of Sciences, Beijing 100190, China; and [c]School of Physical Sciences, University of Chinese Academy of Sciences, Beijing 100049, China

Author contributions: D.W., M.Y., J.Y., and Y.P. designed research; Y.L., and D.W. performed experiments; L.L. performed modeling; D.W., M.Y., and J.Y. contributed new reagents/analytic tools; Y.L., R.H., D.W., and L.L. analyzed data; and D.W. and L.L. wrote the paper.

1. E. Védie, H. Brisset, J. F. Briand, C. Bressy, Bioinspiration and microtopography as nontoxic strategies for marine bioadhesion control. *Adv. Mater. Interfaces* **8**, 2100994 (2021).
2. A. G. Nurioglu, A. C. C. Esteves, G. de With, Non-toxic, non-biocide-release antifouling coatings based on molecular structure design for marine applications. *J. Mater. Chem. B* **3**, 6547–6570 (2015).
3. P. Y. Qian, A. Cheng, R. Wang, R. Zhang, Marine biofilms: Diversity, interactions and biofouling. *Nat. Rev. Microbiol.* **20**, 671–684 (2022).
4. P. D. Frymier, R. M. Ford, H. C. Berg, P. T. Cummings, Three-dimensional tracking of motile bacteria near a solid planar surface. *Proc. Natl. Acad. Sci. U.S.A.* **92**, 6195–6199 (1995).
5. A. P. Berke, L. Turner, H. C. Berg, E. Lauga, Hydrodynamic attraction of swimming microorganisms by surfaces. *Phys. Rev. Lett.* **101**, 038102 (2008).
6. G. Li, J. X. Tang, Accumulation of microswimmers near a surface mediated by collision and rotational brownian motion. *Phys. Rev. Lett.* **103**, 078101 (2009).
7. S. Bianchi, F. Saglimbeni, R. Di Leonardo, Holographic imaging reveals the mechanism of wall entrapment in swimming bacteria. *Phys. Rev. X* **7**, 011010 (2017).
8. G. Junot *et al.*, Run-to-tumble variability controls the surface residence times of *E. coli* bacteria. *Phys. Rev. Lett.* **128**, 248101 (2022).
9. K. Drescher, J. Dunkel, L. H. Cisneros, S. Ganguly, R. E. Goldstein, Fluid dynamics and noise in bacterial cell–cell and cell–surface scattering. *Proc. Natl. Acad. Sci. U.S.A.* **108**, 10940–10945 (2011).
10. K. Schaar, A. Zöttl, H. Stark, Detention times of microswimmers close to surfaces: Influence of hydrodynamic interactions and noise. *Phys. Rev. Lett.* **115**, 038101 (2015).
11. E. Perez Ipiña, S. Otte, R. Pontier-Bres, D. Czerucka, F. Peruani, Bacteria display optimal transport near surfaces. *Nat. Phys.* **15**, 610–615 (2019).
12. T. E. P. Kimkes, M. Heinemann, How bacteria recognise and respond to surface contact. *FEMS Microbiol. Rev.* **44**, 106–122 (2020).
13. H. C. Berg, *Random Walks in Biology* (Princeton University Press, Princeton, N.J.), New and expanded edition edition, p. 152 (1993). Includes bibliographical references (p. [145]-148) and index.
14. D. Wei *et al.*, Confinement reduces surface accumulation of swimming bacteria. *Phys. Rev. Lett.* **135**, 188401 (2025).
15. G. T. Macfarlane, S. Macfarlane, G. R. Gibson, Validation of a three-stage compound continuous culture system for investigating the effect of retention time on the ecology and metabolism of bacteria in the human colon. *Microb. Ecol.* **35**, 180–187 (1998).
16. J. Breton *et al.*, Gut commensal *E. coli* proteins activate host satiety pathways following nutrient-induced bacterial growth. *Cell Metab.* **23**, 324–334 (2016).
17. G. Ariel, A. Be'er, A. Reynolds, Chaotic model for lévy walks in swarming bacteria. *Phys. Rev. Lett.* **118**, 228102 (2017).
18. J. Y. Tinevez *et al.*, Trackmate: An open and extensible platform for single-particle tracking. *Methods* **115**, 80–90 (2017).
19. M. Molaei, M. Barry, R. Stocker, J. Sheng, Failed escape: Solid surfaces prevent tumbling of *Escherichia coli*. *Phys. Rev. Lett.* **113**, 068103 (2014).
20. I. D. Vladescu *et al.*, Filling an emulsion drop with motile bacteria. *Phys. Rev. Lett.* **113**, 268101 (2014).
21. S. Espada Burriel, R. Colin, Active density pattern formation in bacterial binary mixtures. *PRX Life* **2**, 023002 (2024).
22. P. H. Htet, D. Das, E. Lauga, Hydrodynamic hovering of swimming bacteria above surfaces. *Phys. Rev. Res.* **6**, L032070 (2024).
23. E. Lauga, W. R. DiLuzio, G. M. Whitesides, H. L. Stone, Swimming in circles: Motion of bacteria near solid boundaries. *Biophys. J.* **90**, 400–412 (2006).
24. S. Kamdar *et al.*, Multiflagellarity leads to the size-independent swimming speed of peritrichous bacteria. *Proc. Natl. Acad. Sci. U.S.A.* **120**, e2310952120 (2023).
25. B. Zhang, P. Leishangthem, Y. Ding, X. Xu, An effective and efficient model of the near-field hydrodynamic interactions for active suspensions of bacteria. *Proc. Natl. Acad. Sci. U.S.A.* **118**, e2100145118 (2021).
26. P. Leishangthem, X. Xu, Thermodynamic effects are essential for surface entrapment of bacteria. *Phys. Rev. Lett.* **132**, 238302 (2024).
27. D. Wei *et al.*, Scaling transition of active turbulence from two to three dimensions. *Adv. Sci.* **11**, 2402643 (2024).
28. A. Tao, S. Fu, R. Zhang, J. Yuan, Flagellar location determines the stability of bacterial surface entrapment. *Proc. Natl. Acad. Sci. U.S.A.* **122**, e2506380122 (2025).
29. Q. Wang *et al.*, Untethered miniature robots for minimally invasive thrombus treatment: From bench to clinical trials. *Innovation* **6**, 100874 (2025).
30. D. Liu, T. Wang, Y. Lu, Untethered microrobots for active drug delivery: From rational design to clinical settings. *Adv. Healthc. Mater.* **11**, 2102253 (2022).
31. Y. Liu *et al.*, Data for "Crowding limits relative bacterial surface accumulation with density-induced effective heating." Figshare. https://doi.org/10.6084/m9.figshare.30907529. Deposited 13 October 2026.

Downloaded from https://www.pnas.org by CAS INSTITUTE OF PHYSICS on October 30, 2026 from IP address 159.226.35.209.